JOURNAL OF SOLID STATE CHEMISTRY 119, 246–253 (1995)

Copper–Zinc–Cobalt–Chromium Hydroxycarbonates and Oxides

Simone Morpurgo, Mariano Lo Jacono, and Piero Porta[1]

Centro del Consiglio Nazionale delle Ricerche (CNR) su "Struttura e Attività Catalitica di Sistemi di Ossidi" (SACSO), Dipartimento di Chimica, Università La Sapienza, Piazzale Aldo Moro 5, 00185 Rome, Italy

Received November 28, 1994; in revised form May 8, 1995; accepted May 9, 1995

Hydroxycarbonate precursors with different Cu/Zn/Co/Cr atomic ratios and Cu–Zn–Co–Cr oxides obtained by thermal treatment of the precursors at different temperatures (623, 723, and 973 K in air) have been examined. Characterization has been performed by X-ray powder diffraction, diffuse reflectance spectroscopy, thermal analysis, surface area determination, and measurement of magnetic susceptibility. X-ray diffraction patterns show that the precursors are essentially hydrotalcite-like materials with the general formula $(M^{2+})_6(M^{3+})_2(OH)_{16}CO_3 \cdot 4H_2O$ (M^{2+} = Cu, Zn, Co; M^{3+} = Cr). Thermal decomposition of the precursors occurs in four steps; the first three (up to $T = 623$ K) consist of complete dehydration of the sample, and the fourth ($623 \leq T \leq 773$ K) is due to the release of CO_2. The precursor structure collapses at $T \leq 623$ K, giving rise to nearly amorphous materials. Crystalline oxide mixtures are formed only after complete release of CO_2. X-ray diffraction patterns show that the oxides obtained by calcination of 973 K consist of a mixture of CuO, ZnO, and $ZnCr_2O_4$–$ZnCo_2O_4$–Co_3O_4 spinel solid solutions. According to reflectance spectroscopy and magnetic susceptibility measurements, the inclusion of Zn^{2+} and Co^{3+} ions in the spinel-like solid solution seems to be privileged with respect to the formation of separate Co_3O_4 and ZnO phases.

INTRODUCTION

The copper/zinc oxide catalyst containing alumina or chromia is industrially important for methanol synthesis from H_2 and CO (1–6). It has been reported that the mixed catalysts are much more active than each of the components and that the activity is enhanced if great homogeneity of the oxides is achieved. Materials which satisfy such requirements are preferably derived by thermal decomposition of suitable precursors containing all of the metal cations in the same phase (7, 8).

It has also been shown that addition of cobalt to Cu/ZnO/M_2O_3 catalysts results in a better selectivity towards the formation of higher alcohols and hydrocarbons with respect to methanol (9–13).

The aim of this work, which follows that already published on the Cu–Zn–Co–Al system (14), was to synthesize hydrotalcite-type[2] precursors containing an intimate mixture of many metals (Cu^{2+}, Zn^{2+}, Co^{2+}, Cr^{3+}) in the same framework of the layered double hydroxyde (LDH) structure, to define the thermal stability and the structural and electronic properties of the precursors as functions of the metal composition, and to study the structural, magnetic, and electronic properties of the oxides produced by thermal treatment of the precursors. The M^{2+}/M^{3+} ratio has been kept equal to 3 in each sample in order to obtain monophasic hydrotalcite-like compounds. The Cu/Zn ratio is also constant and close to 2.3. The content of cobalt, which is added at expense of copper and zinc, ranges from 0 to 15 mole%. The study has been performed with the aid of several complementary techniques such as X-ray powder diffraction (XRPD), diffuse reflectance spectroscopy, thermal analysis, magnetic susceptibility, and BET surface area determination.

EXPERIMENTAL

Preparation

The hydroxycarbonate precursors were prepared by addition of 0.5 liter of a 0.6 mole liter^{-1} solution containing the metal nitrates to 1 liter of a 0.67 mole liter^{-1} $NaHCO_3$ solution at a constant temperature of 313 K and under vigorous stirring. The slurry was digested for 2 hr under the same conditions. The pH after precipitation was ca. 6.5. From time to time it was adjusted by dropwise addition of a 1 mole liter^{-1} NaOH solution, until the final value was ca. 8. The color of the slurry was blue-green. The precipitate was washed with 10 liters of distilled water in order to eliminate the excess of Na^+ and NO_3^- ions. After washing, the precipitate was dried in vacuum at room temperature for 4–5 days using anhydrous $CaCl_2$ as a

[1] To whom correspondence should be addressed.

[2] The mineral rhombohedral hydrotalcite (*Hy*) has the formula $Mg_6Al_2(OH)_{16}CO_3 \cdot 4H_2O$ and a structure consisting, as shown in the perspective view of Fig. 1, of positively charged brucite-like layers (in which all cations are randomly distributed among the octahedral positions) with the interlayer space filled with anions and water molecules (15).

0022-4596/95 $12.00

TABLE 1

Analytical and Nominal (in Brackets) Metal Molar % Composition (Estimated Experimental Error: ±2%), Phases Detected by XRPD in the Precursors and in the Oxides Calcined at 973 K, Surface Areas (ϕ) of the Samples Calcined at 723 and 973 K, Phase Composition (Weight %) of the Oxides Calcined at 973 K, Phase Composition (Molar %) of the Spinels, Observed (a_o, with e.s.d.'s in Parentheses), and Calculated (a_c, Estimated Error: 1%) Lattice Parameter, Observed (χ_o) and Calculated (χ_{calc}) Magnetic Susceptibility per Gram of Sample

Cobalt content	Co = 0	Co = 5	Co = 10	Co = 15
Cu%	56.0 (52.5)	51.1 (49.0)	47.6 (45.5)	44.7 (42.0)
Zn%	17.9 (22.5)	18.7 (21.0)	17.9 (19.5)	16.4 (18.0)
Co%		4.3 (5.0)	9.0 (10.0)	13.9 (15.0)
Cr%	26.1 (25.0)	25.9 (25.0)	25.5 (25.0)	25.0 (25.0)
Precursor phases[a]	*Hy* (+*M*)	*Hy* (+*M*)	*Hy* (+*M*)	*Hy*
Oxide phases (973 K)[a]	*T*, *Z*, *S*	*T*, *Z*, *S*	*T*, *Z*, *S*	*T*, *S*
ϕ/m^2 g^{-1} (723 K)	36	44	45	50
ϕ/m^2 g^{-1} (973 K)	14	13	12	11
Oxide composition				
CuO	56.4	51.6	47.7	44.7
ZnO	5.0	3.7	2.0	—
Spinel	38.6	44.7	50.3	55.2
Spinel composition				
$ZnCr_2O_4$	100	85.8	75.9	67.8
$ZnCo_2O_4$	—	14.2	18.8	21.2
Co_3O_4	—	—	5.3	11.0
Spinel lattice parameter				
a_o/Å	8.328 (1)	8.291 (1)	8.264(1)	8.246 (1)
a_c/Å	8.327	8.294	8.270	8.251
Magnetic susceptibility				
χ_o (emu $\times 10^6$)[b]	22.3	20.1	18.8	17.9
χ_{calc} (emu $\times 10^6$)[b]	22.3[c]	18.9	18.3	18.1

[a] Symbols: *Hy* = hydrotalcite, *M* = malachite, *T* = tenorite, *Z* = zincite, *S* = spinel.
[b] SI unit = $4\pi 10^{-3}$ emu.
[c] Experimental value for the reference compound $ZnCr_2O_4$.

dehydratant. The dry product was finely ground in an agate mortar. The content of residual Na^+ was analyzed by atomic absorption and found to be less than 0.05% in weight. The color of the compounds was light green.

The major problem connected with the precursor synthesis was the complementary formation of small amounts of $Cu_2(OH)_2CO_2$ (malachite) as a byproduct. We found, in general, that the presence of malachite in the precipitate was promoted by (i) high final pH values (≥8–8.5), (ii) excess of $NaHCO_3$, (iii) high temperature of the slurry (≥323 K), and (iv) long digestion time. Moreover, the coprecipitation process tended to yield quasi-amorphous compounds if operated from highly supersaturated solutions. The experimental parameters (pH, amount of $NaHCO_3$ employed, temperature, digestion time) were adjusted in order to minimize the content of malachite and to obtain monophasic LDH-type precursors.

The oxides were obtained by calcination of the corresponding precursors for 6 hr in air at different temperatures (623, 723, and 973 K).

Techniques

Metals analysis was performed by atomic absorption on the oxides obtained by calcination at 973 K. The samples, whose solubilization turned out extremely difficult even in strongly acidic solution, were previously melted with $KHSO_4$ in a Pt crucible. Analytical results are given in Table 1, together with the nominal composition (in brackets).

X-ray powder diffraction patterns were obtained with a Philips automated PW 1729 diffractometer equipped with an IBM PS2 computer for data acquisition and analysis (software APD-Philips) and an HP Plotter. Scans were taken with a 2θ step size of 0.01° and using Cu$K\alpha_1$ (nickel-filtered) radiation. XRPD data for reference hydroxycarbonates and oxides were taken from ref. (16). Table 1 reports the phases detected for each precursor and calcined (973 K) sample.

The thermal behavior of the precursors was determined with a Stanton Redcroft STA-781 simultaneous TGA-DTA apparatus (Pt crucibles, Pt–Pt/Rh thermocouples,

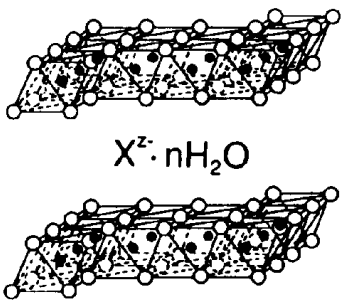

FIG. 1. Perspective view of the hydrotalcite, $Mg_6Al_2(OH)_{16}CO_3 \cdot 4H_2O$, framework. ●: Mg^{2+} or Al^{3+}; O: hydroxyl; X^{z-}: anion.

heating rate 10 K min^{-1}), 15–20 mg of sample being employed for the runs.

Diffuse reflectance spectra (DRS) were taken in the wavelength range 4000–50,000 cm^{-1} with a Varian CARY 2300 specrometer equipped with an IBM PS2 computer for data acquisition and analysis (software Spectra Cal.–Galactic Industries Corp.), and using PTFE as reference.

The total surface area of the oxide mixtures (obtained at 723 and 973 K) was measured by the BET method using nitrogen as adsorbate.

The magnetic susceptibilities were measured using the Gouy method at room temperature.

RESULTS AND DISCUSSION

Hydroxycarbonate Precursors

The XRPD patterns of the precursors are reported in Fig. 2. In spite of some broadening of the peaks, they correspond to the typical pattern of the layered hydrotalcite-like compounds (16a), in which the equally spaced peaks are due to the (001) reflections. The patterns show a slight decrease of crystallinity with increasing cobalt content.

The samples with cobalt content equal to 0, 5, and 10 mole% show, in addition to hydrotalcite, the presence of a small amount of malachite, $Cu_2(OH)_2Co_3$ (16b), whose strongest lines are indicated by full points in Fig. 2.

The position of the peaks related to the (001) reflections of the hydrotalcite-like structure does not change with varying cobalt content. This is in substantial agreement with the structural model of the LDH material (Fig. 1), whose interlayer distance along the c axis is mostly due to the size and the shape of the charge-balancing anion rather than to the size of the cations contained in the layers.

The reflectance spectra of the Cu–Zn–Co–Cr-containing precursors are reported in Fig. 3 (c–f). The (a) and (b) spectra are reported for comparison and correspond to $Zn_6Cr_2(OH)_{16}CO_3 \cdot 4H_2O$ and $Cu_2Zn_4Al_2(OH)_{16}CO_3 \cdot 4H_2O$, respectively, compounds synthesized in our laboratory and containing Cr^{3+} and Cu^{2+} as the only spectroscopically active species. The DR spectra of the hydroxycarbonate precursors show (Fig. 3 c–f) (i) a shoulder at ca. 8500 and a broad band at ca. 12,500 cm^{-1} corresponding to the expected transitions for Cu^{2+} in a distorted octahedral (O_h) coordination (17, 18); (ii) a shoulder at ca. 17,500 cm^{-1} due to the $^4A_{2_g} \rightarrow {}^4T_{2_g}$ transition of O_h-Cr^{3+} (17); (iii) a slightly visible band at ca. 24,500 cm^{-1} corresponding to the $^4A_{2_g} \rightarrow {}^4T_{1_g}(F)$ spin-allowed transition of O_h-Cr^{3+}. Note that the $^4A_{2_g} \rightarrow {}^4T_{1_g}(P)$ spin-allowed transition of O_h-Cr^{3+} is hidden by a strong charge-transfer band which starts at ca. 25,000 cm^{-1}, and that the transitions of O_h-Co^{2+} (expected at ca. 8000 and 20,000 cm^{-1}) (19) are covered by the absorption of Cu^{2+} and Cr^{3+}.

The thermal analysis (TG and DTA) of the hydroxycarbonate precursors has been performed in air up to 973 K. Figure 4 shows, as an example, the thermal features for

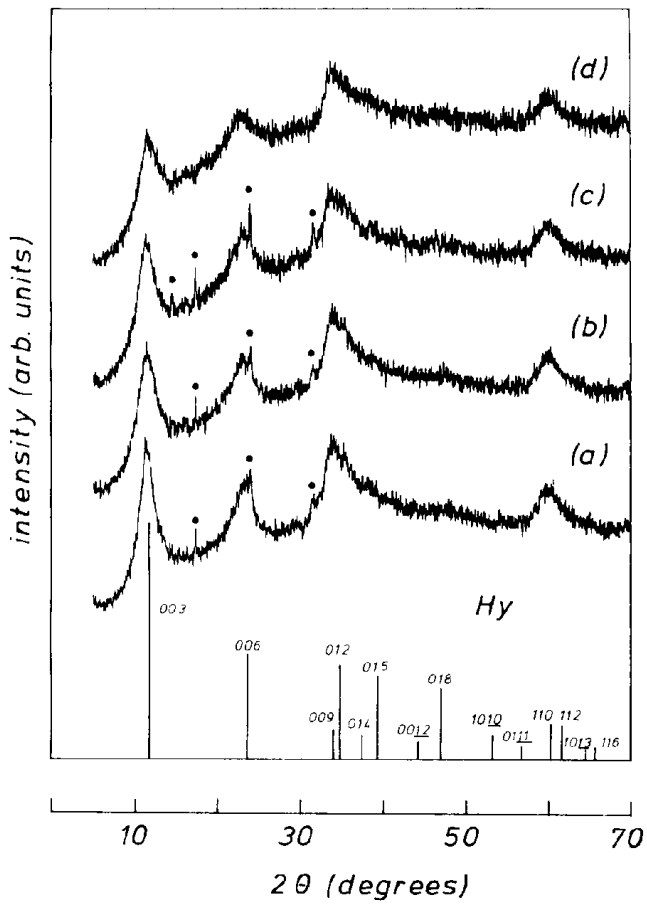

FIG. 2. XRPD patterns (Cu-$K\alpha_1$ radiation) for Cu–Zn–Co–Cr precursors with different cobalt content: (a) Co = 0; (b) Co = 5; (c) Co = 10; (d) Co = 15. ●: strongest lines for malachite, $Cu_2(OH)_2CO_3$. At the bottom, the lines, with Miller (hkl) indices and relative intensities, are given for hydrotalcite-like, H_y, $Cu_2Zn_4Al_2(OH)_{16}CO_3 \cdot 4H_2O$ reference compound (16a).

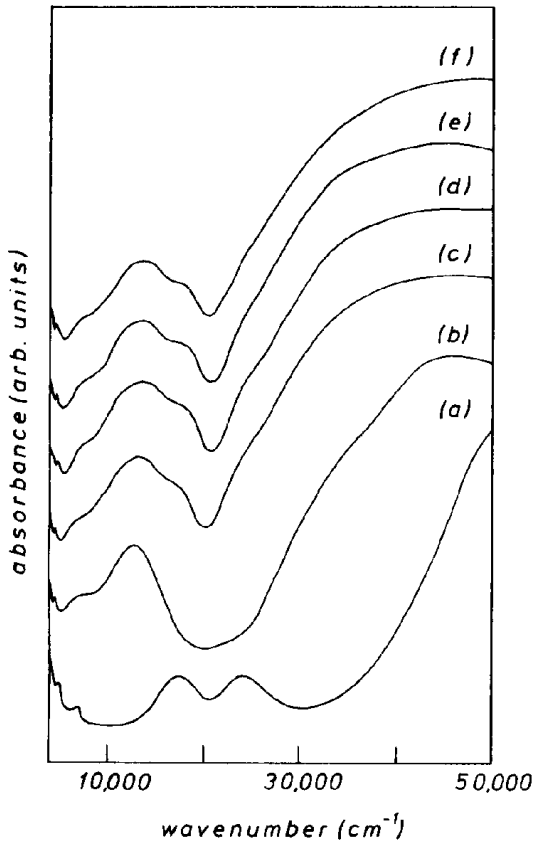

FIG. 3. Reflectance spectra: (a) $Zn_6Cr_2(OH)_{16}CO_3 \cdot 4H_2O$ reference compound; (b) $Cu_2Zn_4Al_2(OH)_{16}CO_3 \cdot 4H_2O$ reference compound; (c)precursor with Co = 0; (d) Co = 5; (e) Co = 10; (f) Co = 15.

the sample Co = 0 (the thermograms are similar for all precursors). The thermal decomposition of the samples, independently of their Cu–Zn–Co–Cr relative content, occurs through the following four steps (% weight loss, Δp, in parentheses):

(i) $T \leq 363$–373 K, loss of the residual water adsorbed on the surface of the sample ($\Delta p \simeq 1.5\%$);

(ii) $373 \leq T \leq 423$ K, loss of the crystallization water ($\Delta p \simeq 8\%$) located between the positively charged layers, corresponding to the process:

$$(M^{2+})_6(M^{3+})_2(OH)_{16}CO_3 \cdot 4H_2O(s) \rightarrow (M^{2+})_6(M^{3+})_2(OH)_{16}CO_3(s) + 4H_2O(g);$$

(iii) $423 \leq T \leq 623$ K, dehydration of the brucite-like layers ($\Delta p \simeq 16\%$) due to the reaction:

$$(M^{2+})_6(M^{3+})_2(OH)_{16}CO_3(s) \rightarrow (M^{2+})_6(M^{3+})_2O_8CO_3(s) + 8H_2O(g);$$

(iv) $623 \leq T \leq 773$ K, release of CO_2 ($\Delta p \simeq 5\%$), leading to the formation of the M^{2+}–M^{3+} containing oxides.

The experimental weight loss of each step agrees with the value calculated according to the structural formula of the LDH compound. Note that (i) the second and the third steps can be distinguished from a slope change in the TG curve; (ii) the first two endothermic peaks (at 383 and 523 K) observed in the DTA plot correspond to the second and third steps of the thermal decomposition, respectively; (iii) the third endothermic peak at 733 K and the exothermic one at 783 K are respectively associated to the release of CO_2 and to the formation of crystalline oxides. In the window of Fig. 4 it is additionally shown that with increasing cobalt content CO_2 tends to be lost at slightly lower temperatures (an inverse tendency is noted for the samples with Co = 10 and Co = 15). The temperature of the dehydration process is not affected by the cobalt content.

The easier release of CO_2 in cobalt-containing materials seems to indicate either that the metal–hydroxide framework as a whole (Fig. 1) becomes less positive when cobalt replaces both copper and zinc (so retaining less strongly the interlayering carbonate anion), or, more likely, that the cobalt-containing oxides are formed at a lower temperature than the other oxides.

Oxides

The XRPD patterns of the sample Co = 0, calcined for 6 hr at different temperatures are reported in Fig. 5. The spectrum of the sample calcined at 623 K (Fig. 5a) shows a quasi-amorphous structure with the absence of the X-ray lines of the hydroxycarbonate precursors. The very

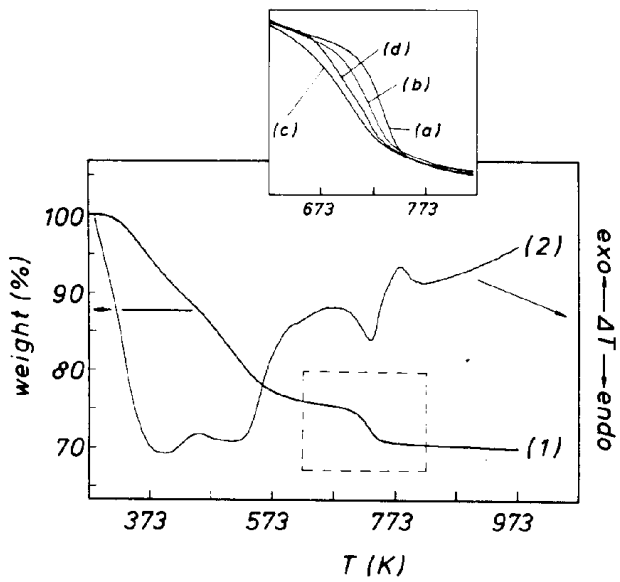

FIG. 4. Thermal analysis for the precursor with Co = 0: (1) TGA, (2) DTA. Window (top): TGA for precursors with different cobalt content: (a) Co = 0; (b) Co = 5; (c) Co = 10; (d) Co = 15.

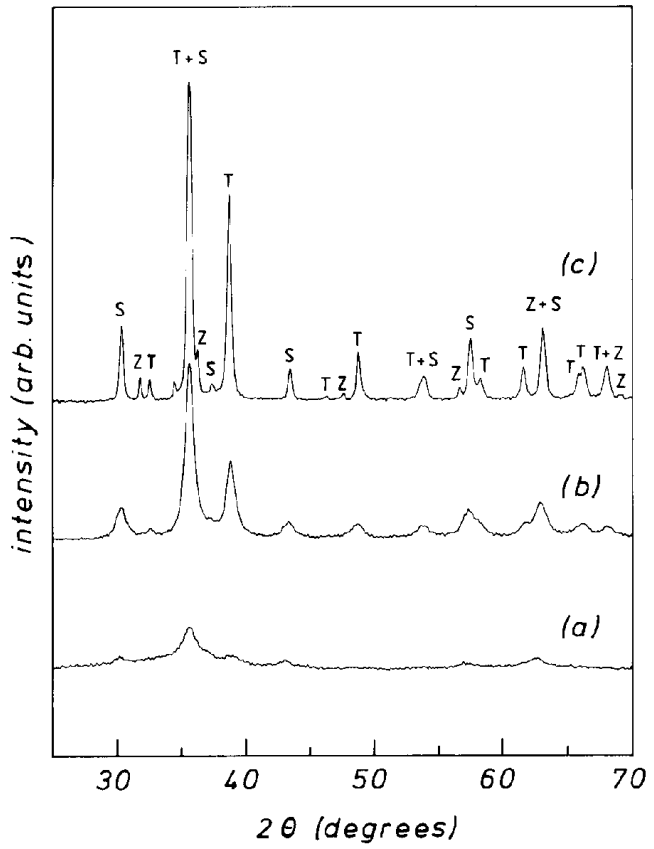

FIG. 5. XRPD patterns (Cu$K\alpha_1$ radiation) for the sample with Co = 0 calcined at different temperature: (a) 623 K; (b) 723 K; (c) 973 K. The phases observed at the final temperature (973 K) are indicated as follows: T = tenorite, Z = zincite, S = spinel.

weak bands correspond to the lines of CuO and of a spinel phase. In accordance with the thermal analysis, it may be deduced that the complete dehydration of the precursors at 623 K leads to the oxycarbonate materials, $(M^{2+})_6(M^{3+})_2O_8CO_3$, where an incipient formation of oxide microdomains arises within the layers.

The XRPD pattern of the sample calcined at a higher temperature (723 K, Fig. 5b) reveals the unequivocal presence of CuO and spinel. The increase in the temperature and the almost complete release of CO_2 thus allows a further nucleation of the oxide microdomains, although, at this temperature, the system is not yet highly crystalline. The further calcination at 973 K (Fig. 5c) results in the formation of highly crystalline CuO, ZnO, and $ZnCr_2O_4$.

The cobalt-containing samples have shown a quite similar trend as a function of the calcination temperature.

The XRPD patterns of the samples having different cobalt content, calcined for 6 hr at 973 K, are reported in Fig. 6. They generally reveal the presence of CuO, ZnO, and spinel-like phase.

With increasing cobalt content, the following features arise from a qualitative analysis of the X-ray diffraction patterns: (i) the relative peak intensity of CuO and specially of ZnO decreases (no ZnO is detectable in the sample Co = 15); (ii) the relative peak intensity of the spinel phase increases; (iii) the reflections related to the spinel phase are progressively shifted to higher 2θ angles. As an example, it is visible from Fig. 6 (namely Figs. 6a and 6d) that the (311) reflection of the spinel phase and the (002)/($\bar{1}$11) reflection of CuO are superimposed (at $2\theta \approx 35.6°$) in the sample with Co = 0, whereas they are well resolved in the sample with Co = 15.

Points (i) and (ii) can be explained by first taking into account that the total amount of copper and zinc in the samples decreases with increasing cobalt content (see Table 1). Moreover, the strong dominution of ZnO and the growth of the spinel phase are due to the formation of zinc cobaltite, $ZnCo_2O_4$, a very stable spinel which is usually formed at a lower temperature (723 K) (16h) than other parent spinels. Point (iii), as will be discussed later,

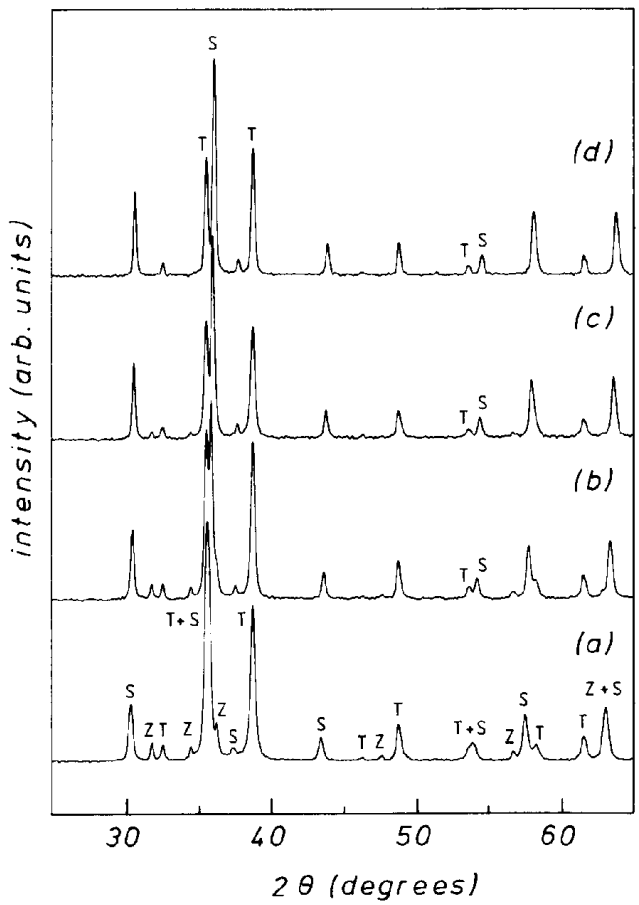

FIG. 6. XRPD patterns (Cu$K\alpha_1$ radiation) for samples at different cobalt content calcined at 973 K: (a) Co = 0; (b) Co = 5; (c) Co = 10; (d) Co = 15. The observed phases are indicated as follows: T = tenorite, Z = zincite, S = spinel.

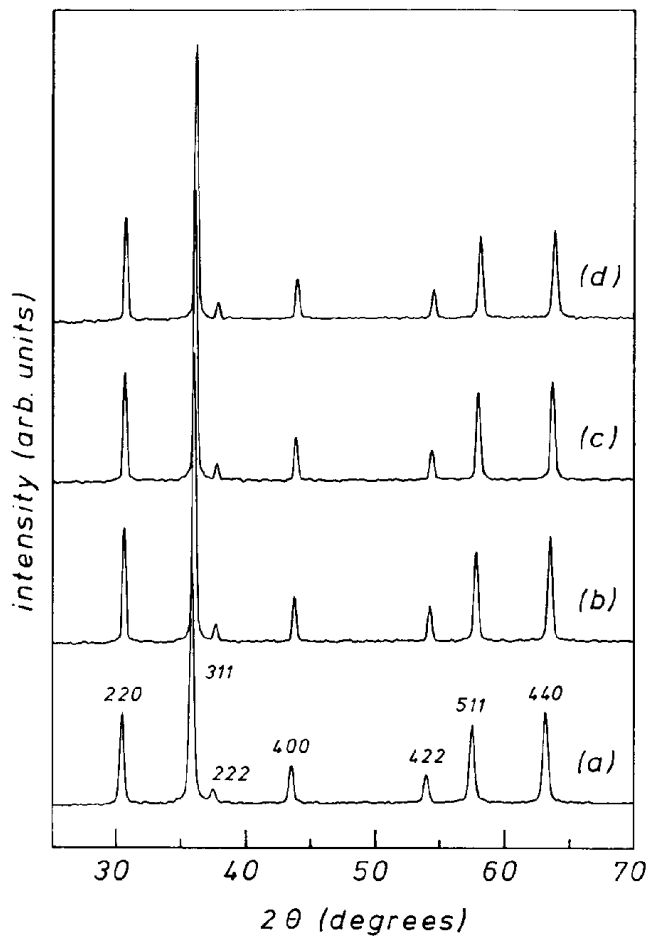

FIG. 7. XRPD patterns (Cu$K\alpha_1$ radiation) for samples at different cobalt content, calcined at 973 K and washed with dilute HCl: (a) Co = 0; (b) Co = 5; (c) Co = 10; (d) Co = 15. The Miller (*hkl*) indices are given for the spinel phase.

can be accounted for by the formation of a solid solution between different spinels.

In order to allow a more accurate analysis of the X-ray reflections belonging to the spinel phases (without the interference of CuO and ZnO) the samples calcined at 973 K were washed with a cold and dilute HCl solution which completely removed CuO and ZnO. Note that the analysis of copper in the washed samples revealed a very low Cu content (~1% in for all samples) in the spinel phase, indicating that the materials obtained after HCl treatment consist essentially of a mixture of Zn–Cr–Co-containing (copper-free) spinel phase.

The XRPD patterns of the washed samples are shown in Fig. 7. The observed lattice parameter of the cubic spinel, a_0 (determined from the position of the X-ray reflections observed up to $2\theta = 70°$), was found to decrease linearly with increasing Co content (see Table 1).

By taking into account the analytical composition of the samples and assuming the formation of spinel solid solutions, the values of the lattice parameters were calculated for each sample at different cobalt content [$a_c = \Sigma_i X_i a_i$, where a_i is the value quoted in the literature for the ith phase, i.e., 8.3275, 8.0946, and 8.084 Å for $ZnCr_2O_4$ (16e), $ZnCo_2O_4$ (16h), and Co_3O_4 (16i), respectively, and X_i the corresponding molar fraction]. It may be seen from Table 1 that the a_c values are in good agreement with the observed ones.

According to the previous findings we could thus infer that (i) copper is essentially present in all samples as CuO; (ii) the decrease of the amount of ZnO with the increase in cobalt content signifies that Zn^{2+} ions are more and more involved in the formation of the spinel phase; (iii) for the sample without cobalt, $ZnCr_2O_4$ is, as expected, the only spinel formed; (iv) the addition of cobalt produces first (sample with Co = 5) a $Zn[Cr^{3+}_{2-y}Co^{3+}_y]O_4$ ternary spinel solid solution (both Co^{3+} and Cr^{3+} located at the O_h sites of the structure), and next (samples with Co = 10 and 15) a $Zn_{1-x}Co^{2+}_x[Cr^{3+}_{2-y}Co^{3+}_y]O_4$ quaternary spinel solid solution. Co^{2+} and Zn^{2+} are present in the tetrahedral (T_d) sites of the spinel structure, as observed in $CoCr_2O_4$ and $ZnCr_2O_4$ (20).

The results obtained by XRPD analysis are confirmed by reflectance spectroscopy and magnetic measurements.

The DR spectra of the samples with different cobalt content calcined for 6 hr at 973 K, not shown here, were dominated by the strong absorption threshold of CuO at ca. 12,500 cm^{-1} (21). The other relevant spectroscopic features, related to the presence of the spinel phase, are better evidenced in the spectra of the corresponding samples treated with dilute HCl (Fig. 8b–8e), where the interference of CuO has been removed. The sample without cobalt shows (Fig. 8b), in the near infrared region (4000–10,000 cm^{-1}), a broad band whose shape cannot easily be ascribed to any *d–d* transition, but more likely is due to the presence of cation vacancies in the defective $Zn_{1-x}Cr_{2-y}O_4$ spine structure. This band becomes narrower with increasing cobalt content (Fig. 8c, 8d) and is replaced, at the highest cobalt content (Fig. 8d), by a structured band centered at ca. 7000 cm^{-1}, which corresponds to the $^4A_2 \rightarrow {}^4T_1(F)$ transition of T_d Co^{2+} (19, 24). We can thus infer that the vacancies are progressively filled by the inclusion of some cobalt in both T_d (Co^{2+}) and O_h (Co^{3+}) sites, giving rise to quaternary $Zn_{1-x}Co^{2+}_x[Cr^{3+}_{2-y}Co^{3+}_y]O_4$ less defective spinels.

In addition to the band in the near infrared region, the sample with Co = 0, Fig. 8b, shows a small band at ca. 14,500 cm^{-1} and two absorptions centered at 17,500 and 24,000 cm^{-1}. These three bands correspond to the transitions from the ground state, $^4A_{2g}$, to the higher $^2E_g/{}^2T_{2g}$, $^4T_{2g}$, and $^4T_{1g}$ states, respectively, of O_h Cr^{3+} (in Cr/Al_2O_3 these bands occur at 14,430, 18,000, and 24,600 cm^{-1}, respectively) (17). Note that Fig. 8a shows for comparison the spectrum of $ZnCr_2O_4$ used as a reference for the spec-

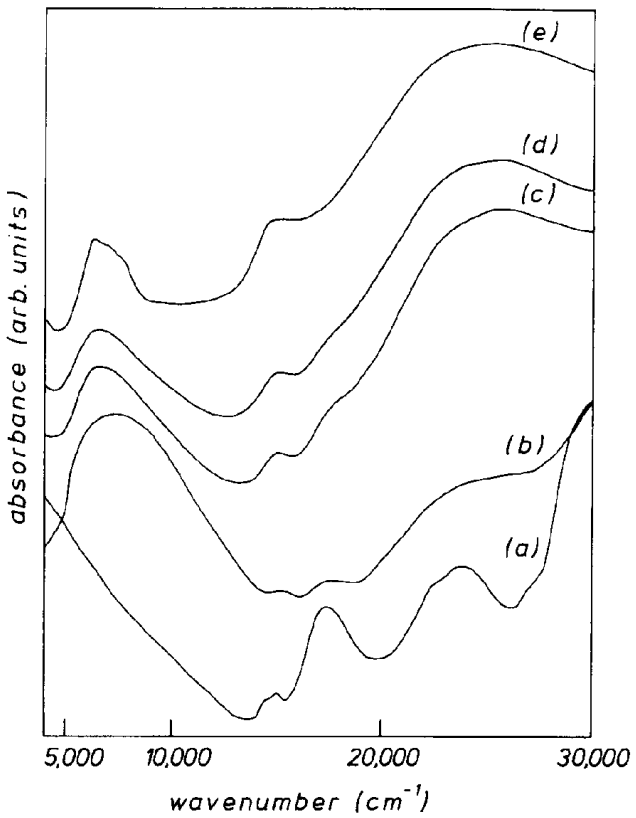

FIG. 8. Reflectance spectra for samples at different cobalt content, calcined at 973 K and washed with dilute HCl: (b) Co = 0; (c) Co = 5; (d) Co = 10; (e) Co = 15. Spectrum (a) is reference $ZnCr_2O_4$.

troscopic transitions of Cr^{3+} in the spinel structure (25). At increasing cobalt content, Fig. 8c–8e, the band at ca. 24,000 cm^{-1} becomes stronger in the presence of O_h Co^{3+} (17).

The observed value of the magnetic susceptibility per gram of sample (χ_0) of the washed materials (identified by XRPD, Fig. 7, as pure spinel solid solutions) decreases with increasing cobalt content (Table 1). This trend can qualitatively be explained considering that the majority of cobalt introduced in the initial $ZnCr_2O_4$ spinel is the diamagnetic Co^{3+} species which replaces the paramagnetic Cr^{3+} one. By taking into account the same spinel phase composition used to estimate the values of the lattice parameters, the magnetic susceptibility has been calculated for each sample according to the expression $\chi_{calc} = \Sigma_i W_i(\chi_{sp})_i$, where $(\chi_{sp})_i$ and W_i are the magnetic susceptibility per gram and weight percent, respectively, of the ith spinel phase believed to be present in the solid solution [χ_{sp} (emu, where SI unit = $4\pi \times 10^{-3}$ emu) used for the different phases: 22.3×10^{-6} for $ZnCr_2O_4$ (measured in our laboratory), -0.31×10^{-6} for $ZnCo_2O_4$ (from the diamagnetic contributions of the single ions) (26), and 30.3×10^{-6} for Co_3O_4 (27)]. The good agreement between χ_0 and χ_{cal} values (Table 1) confirms the deductions drawn from XRD and DRS methods.

CONCLUSIONS

By several complementary techniques the following points have been evidenced:

(i) Precursors are essentially hydroxycarbonate compounds with layered hydrotalcite-like structures and contain in the same hydroxide layers all Cu^{2+}, Zn^{2+}, Co^{2+}, and Cr^{3+} species.

(ii) Precursors undergo a four-step thermal decomposition in which dehydration from the hydroxyde layers occurs at $T \leq 623$ K with formation of nearly amorphous oxycarbonate species; CO_2 is released at $623 \leq T \leq 773$ K, with final formation of crystalline oxide mixtures.

(iii) The oxide products obtained by calcining the precursors at 973 K consist of a mixture of CuO, ZnO, and defective $Zn_{1-x}Cr_{2-y}O_4$ spinel for samples without cobalt, of CuO, ZnO, and ternary $Zn[Cr^{3+}_{2-y}Co^{3+}_y]O_4$ spinel solid solution for those with low cobalt content, and of CuO and quaternary $Zn_{1-x}Co^{2+}_x[Cr^{3+}_{2-y}Co^{3+}_y]O_4$ spinel solid solution for samples with higher cobalt content.

ACKNOWLEDGMENT

We thank Dr. R. Dragone for technical assistance.

REFERENCES

1. K. Klier, *Adv. Catal.* **31,** 243 (1982).
2. R. G. Herman, K. Klier, G. W. Simmons, B. P. Finn, J. B. Bulko, and T. P. Kobylinski, *J. Catal.* **56,** 407 (1979).
3. J. B. Bulko, R. G. Herman, K. Klier, and G. W. Simmons, *J. Phys. Chem.* **83,** 3118 (1979).
4. S. Metha, G. W. Simmons, K. Klier, and R. G. Herman, *J. Catal.* **57,** 339 (1979).
5. K. Shimomura, K. Ogawa, M. Oba, and Y. Kotera, *J. Catal.* **52,** 191 (1978).
6. Y. Okamoto, K. Fukino, T. Imanaka, and S. Teranishi, *J. Phys. Chem.* **87,** 3740 (1983).
7. C. Busetto, G. Del Piero, G. Manara, F. Trifirò, and A. Vaccari, *J. Catal.* **85,** 260 (1984).
8. P. Porta, S. De Rossi, G. Ferraris, M. Lo Jacono, G. Minelli, and G. Moretti, *J. Catal.* **109,** 367 (1988).
9. W. X. Pan, R. Cao, and G. L. Griffin, *J. Catal.* **114,** 447 (1988).
10. P. Courty, G. Durand, E. Freund, and A. Sugier, *J. Mol. Catal.* **17,** 241 (1982).
11. J. E. Baker, R. Burch, and S. E. Golunski, *Appl. Catal.* **53,** 279 (1989).
12. G. Fornasari, S. Gusi, F. Trifirò, and A. Vaccari, *Ind. Eng. Chem. Res.* **26,** 1501 (1987).
13. G. Fornasari, A. D'Huysser, L. Mintchev, F. Trifirò, and A. Vaccari, *J. Catal.* **135,** 386 (1992).
14. S. Morpurgo, M. Lo Jacono, and P. Porta, *J. Mater. Chem.* **4**(2), 197 (1994).
15. R. Allmann, *Acta Crystallogr., Sect. B* **24,** 972 (1968).

16. X-Ray Powder Data File, ASTM-cards No.: (a) 38-487 for hydrotalcite-like $Cu_2Zn_4Al_2(OH)_{16}CO_3 \cdot 4H_2O$; (b) 10-399 for malachite, $Cu_2(OH)_2CO_3$; (c) 5-661 for tenorite, CuO; (d) 36-1451 for zincite, ZnO; (e) 22-1107 for $ZnCr_2O_4$; (f) 26-509 for cubic $CuCr_2O_4$; (g) 34-424 for tetragonal $CuCr_2O_4$; (h) 23-1390 for $ZnCo_2O_4$; (i) 9-418 for Co_3O_4; (l) 10-458 for $CoCr_2O_4$.
17. A. B. P. Lever, *in* "Inorganic Electronic Spectroscopy" (A. B. Lever, Ed.). Elsevier, Amsterdam, 1984.
18. C. J. Ballhausen, *in* "Ligand Field Theory" McGraw Hill, New York, (1962).
19. R. Pappalardo, D. L. Wood, and R. C. Linares, *J. Chem. Phys.* **35,** 2041 (1961).
20. R. J. Hill, J. R. Craig, and G. V. Gibbs, *Phys. Chem. Miner.* **4,** 317 (1979).
21. O. V. Krylov, "Catalysis by Nonmetals." pp. 251 and 258. Academic Press, New York, 1970.
22. F. Trifirò and A. Vaccari, *in* "Symposium on Structure-Activating Relationships in Heterogeneous Catalysis," p. 83. Am. Chem. Soc., Boston, 1990.
23. R. A. Jackson, C. R. A. Catlow, and J. M. Thomas, *Catal. Lett.* **8,** 385 (1991).
24. P. Porta and A. Anichini, *J. Chem. Soc. Faraday 1* **76,** 2448 (1980).
25. R. A. Ford and O. F. Hill, *Spectrochim. Acta* **16,** 1318 (1960).
26. P. W. Selwood, *in* "Magnetochemistry" 2nd ed., p. 78. Interscience, New York, 1964.
27. R. C. Weast and M. J. Astle, Eds., "Handbook of Chemistry and Physics" 63rd ed., p. E-118. CRC Press, Boca Raton, FL, 1982-1983.